

Numerical and analytical approaches to an advection-diffusion problem at small Reynolds number and large Péclet number

Nathaniel J. Fuller* and Nicholas A. Licata†

Department of Natural Sciences, University of Michigan-Dearborn, Dearborn, Michigan 48128

(Dated: July 22, 2022)

Obtaining a detailed understanding of the physical interactions between a cell and its environment often requires information about the flow of fluid surrounding the cell. Cells must be able to effectively absorb and discard material in order to survive. Strategies for nutrient acquisition and toxin disposal, which have been evolutionarily selected for their efficacy, should reflect knowledge of the physics underlying this mass transport problem. Motivated by these considerations, in this paper we consider a two-dimensional advection-diffusion problem at small Reynolds number and large Péclet number. We discuss the problem of mass transport for a circular cell in a uniform far-field flow. We approach the problem numerically, and also analytically through a rescaling of the concentration boundary layer. A biophysically motivated first-passage problem for the absorption of material by the cell demonstrates quantitative agreement between the numerical and analytical approaches.

I. INTRODUCTION

The survival of any microorganism is dependent on its ability to control the movement of nutrients and waste between the cell interior and the external environment. Nutrients must be easily captured and waste easily disposed with minimal metabolic exertion [1]. Factors which determine the efficiency of any material transfer mechanism for gathering and disposing of small molecules include the microscale flow profile surrounding the cell [2], the diffusion coefficient of molecules being transported, and the location of transport receptors on the cell surface [3, 4]. As with any other trait, the physical architecture of the transport receptor arrangement is evolutionarily selected to work efficiently within the particular environment that the organism lives. A more detailed understanding of the mass transport problem for molecules in the extracellular fluid can yield valuable information for discerning why a given architecture is preferable over other possible choices [5].

An example which motivates the current study is understanding the mechanism of toxin disposal by sea urchin embryos [3, 6]. Early in development, microvilli (microscopic cylindrical cell membrane protrusions) on the embryo grow to several microns in length, with transport receptors localized at the tips of the microvilli. This localization may help facilitate more efficient toxin disposal by the embryo. By releasing molecules away from the body of the cell, the chances are reduced that expelled toxins are reabsorbed. In this setting, the mass transport problem for molecules in the extracellular fluid is described an advection-diffusion equation at low Reynolds number and large Péclet number. Interestingly, the characteristic lengthscale for the concentration boundary layer may provide a physical rationale for the length

of the microvilli involved in the toxin transport [7].

Calculating the efficiency of a material transfer mechanism requires the solution of two distinct problems. The first problem is to determine the flow profile of the extracellular fluid. In the present context, the Reynolds number of the flow is much smaller than one, which justifies the use of the Stokes equation for describing microscale flows around individual cells. The second problem is to find a solution of the advection-diffusion equation using the calculated flow profile as input. The solution of the advection-diffusion equation provides the concentration profile governing the average motion of particles dissolved in the fluid. Knowledge of the concentration profile leads directly to information about the probability for a given particle to contact the outer envelope of a cell. Since the absorption of a particle requires that it first make contact with the cell surface, the concentration profile can be used to find a theoretical maximum absorption probability [8].

Although the equations which govern the extracellular flow and diffusion of small molecules are well understood, deriving their solutions or even their approximate solutions is often quite involved [9, 10]. The difficulties faced in finding accurate analytic solutions to the Stokes equation and advection-diffusion equation can make numerical schemes an attractive method for finding flow and concentration profiles [11–13]. In this paper we present both numerical solutions, and an analytic approximation based on a rescaling of the concentration boundary layer.

In what follows we restrict our analysis of the flow profile to the case of a circular object obstructing a uniform two-dimensional flow. This configuration is chosen for several reasons. First, it provides a toy model to mimic the flow around a circular cell moving through a liquid. Second, due to the relative simplicity of the geometry, an analytic solution is known for Stokes equation. This allows us to make progress on an analytic approximation to the associated advection-diffusion equation. Third, the numerical model is simplified by the elimination of a spatial variable while continuing to utilize methods appli-

*email address: nfuller@umich.edu

†email address: licata@umich.edu

cable in a similar three-dimensional problem. Our analysis of the concentration profile focuses on the first-passage probability of a particle in the extracellular fluid being absorbed by the cell [14]. The first-passage probability reveals the theoretical maximum efficiency for the capture of small molecules by the cell [8].

II. MODELING FLUID FLOW

Consider a circular cell moving through water. The motion may be driven by gravity, the bulk motion of the fluid, or flagella. The Reynolds number corresponding to the flow around the cell is generally much less than one. At small Reynolds numbers, the magnitude of the inertial terms in the Navier-Stokes equation become much less than the magnitude of the viscous terms. The disparity in magnitude allows for a linearization of the Navier-Stokes equation into the Stokes equation, which neglects the inertial terms.

The flow profile \mathbf{U} satisfies the Stokes equation

$$\mu \nabla^2 \mathbf{U} - \nabla p = 0 \quad (1)$$

where p is the pressure profile and μ is the dynamic viscosity of water. Since the speed of the flow will be much less than the speed of sound in water, the fluid is considered to be perfectly incompressible and satisfy the incompressibility condition

$$\nabla \cdot \mathbf{U} = 0. \quad (2)$$

Working in plane polar coordinates and defining the dimensionless length $\xi = r/R$, velocity $\mathbf{u} = \mathbf{U}/U_\infty$, pressure $\gamma = p/(\rho U_\infty^2)$, and Reynolds number $Re = (\rho R U_\infty)/\mu$ gives the Stokes equation as the coupled system

$$\frac{1}{Re} \left(\frac{\partial^2 u_\xi}{\partial \xi^2} + \frac{1}{\xi} \frac{\partial u_\xi}{\partial \xi} - \frac{u_\xi}{\xi^2} + \frac{1}{\xi^2} \frac{\partial^2 u_\xi}{\partial \theta^2} - \frac{2}{\xi^2} \frac{\partial u_\theta}{\partial \theta} \right) = \frac{\partial \gamma}{\partial \xi} \quad (3a)$$

$$\frac{1}{Re} \left(\frac{\partial^2 u_\theta}{\partial \xi^2} + \frac{1}{\xi} \frac{\partial u_\theta}{\partial \xi} - \frac{u_\theta}{\xi^2} + \frac{1}{\xi^2} \frac{\partial^2 u_\theta}{\partial \theta^2} + \frac{2}{\xi^2} \frac{\partial u_\xi}{\partial \theta} \right) = \frac{1}{\xi} \frac{\partial \gamma}{\partial \theta} \quad (3b)$$

and the incompressibility condition as

$$\frac{\partial u_\xi}{\partial \xi} + \frac{u_\xi}{\xi} + \frac{1}{\xi} \frac{\partial u_\theta}{\partial \theta} = 0. \quad (4)$$

Two boundary conditions are needed for the case of a two dimensional circular cell obstructing an otherwise uniform flow. At the surface of the cell, a no-slip boundary condition is used where $\mathbf{u}(\xi = 1) = 0$. Far from the cell at radius Q , the flow is considered to move uniformly to the right with velocity one, $\mathbf{u}(\xi = Q) = 1\hat{x}$. The analytic solution of the Stokes equation and incompressibility condition meeting these boundary conditions

is

$$\begin{aligned} u_\xi &= \left[-\frac{\xi^2}{2} + \left(Q^2 + 1 \right) \left(\ln(\xi) - \frac{1}{2} \right) + 1 + \frac{Q^2}{2\xi^2} \right] \frac{\cos(\theta)}{G(Q)} \\ u_\theta &= \left[\frac{3\xi^2}{2} - \left(Q^2 + 1 \right) \left(\ln(\xi) + \frac{1}{2} \right) - 1 + \frac{Q^2}{2\xi^2} \right] \frac{\sin(\theta)}{G(Q)} \end{aligned} \quad (5)$$

where $G(Q) = (Q^2 + 1) \ln(Q) + 1 - Q^2$ [15]. With the analytic solution known, a comparison can be made with a numerical scheme for finding the flow profile.

The linearity of both the Stokes equation and the incompressibility condition warrants the use of linear methods of solution which are comparatively simple with respect to methods used in most fluid dynamics problems where the governing equations are non-linear. The details of the numerical approach, based on the Gauss-Seidel method, are presented in the Appendix. We solve for the flow profile in an annulus with inner radius $\xi = 1$ and outer radius $\xi = 100$. A domain this large is necessary since the outer boundary should be quite far from the origin to properly approximate the desired condition $\mathbf{u}(\xi \rightarrow \infty) \rightarrow 1\hat{x}$ for small Reynolds number flows [15]. The domain is parsed by 300 divisions in both the ξ and θ coordinates. The moving cell is considered to have a radius $40\ \mu\text{m}$ and to travel at $0.4\ \text{mm/s}$, parameters which are characteristic of *Strongylocentrotus purpuratus* embryos [16]. The Reynolds number for the swimming embryo is of order 10^{-2} . Using these parameters and running our MATLAB script on a 3.5 GHz processor until the change in the elements of $\mathcal{X}_{i,j}^k$ are less than 10^{-3} between iterations (see Algorithm 2 in the Appendix for details) produces a solution in about 20 minutes.

The accuracy of the numerical solution produced is tested by comparing it with Eq. (5). Fig. 1 shows the relative error of the magnitude of the velocity field while Fig. 2 shows the absolute error in radians of the direction of the velocity field. Notice that the error in the numerical solution becomes somewhat large as ξ approaches one. This is a sign that the grid spacing is too large at that location to accommodate the change in \mathbf{u} between grid points.

The increased error near the inner boundary may present an issue for some biophysical models where the subject of interest is the fluid motion near the cell surface. To improve the accuracy of the solution near the inner boundary, the radius of the domain can be decreased while leaving the number of grid points unchanged. This effectively creates a finer grid in the area where the solution has larger spatial derivatives. To improve the current model near the inner boundary, we decrease the domain radius from 100 to 20 where the error in the solution for the larger domain is still small (<1%). The values of \mathcal{X} at $\xi = 20$ on the larger domain are used to set the outer boundary conditions on the smaller domain. Algorithm 2 is then used with a domain radius of 20 and the new outer boundary conditions to find a more accurate solution for $\xi < 20$.

Fig. 3 and Fig. 4 show the respective error in speed

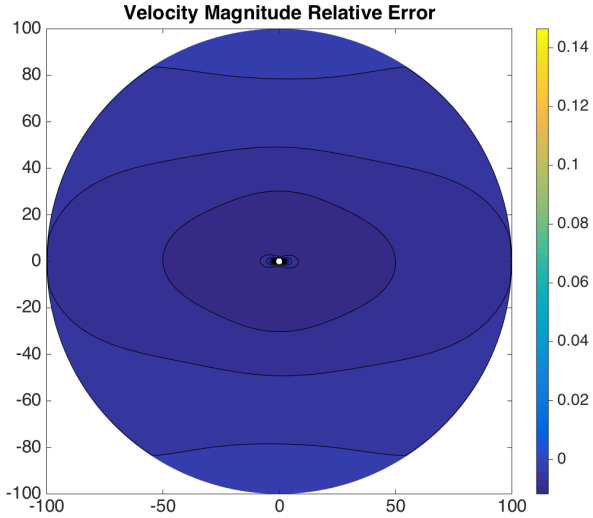


FIG. 1: Relative error of fluid speed for the numerical solution as compared with the analytic solution (Eq. 5). The error is small (< 1%) across most of the domain but becomes larger near the inner boundary.

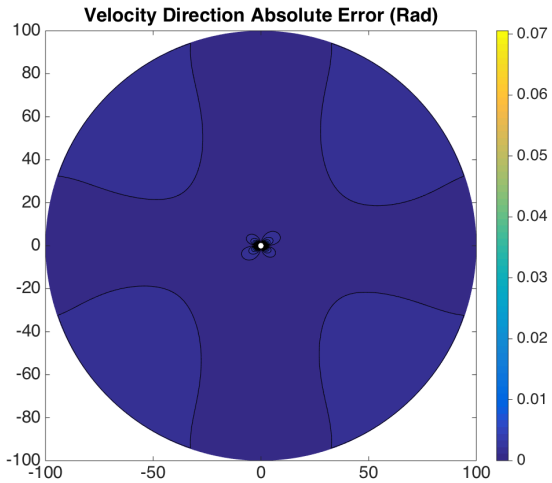


FIG. 2: Absolute error of fluid direction for the numerical solution as compared with the analytic solution (Eq. 5). The error is small (< 1%) across most of the domain but becomes larger near the inner boundary.

and direction of the fluid profile generated on a domain of radius 20. The areas of error larger than 1% are smaller in size and the maximum error at any point on the domain has also decreased.

III. MODELING ADVECTION AND DIFFUSION

With a solution for the flow profile in hand, we now turn to the second problem, determining the concentra-

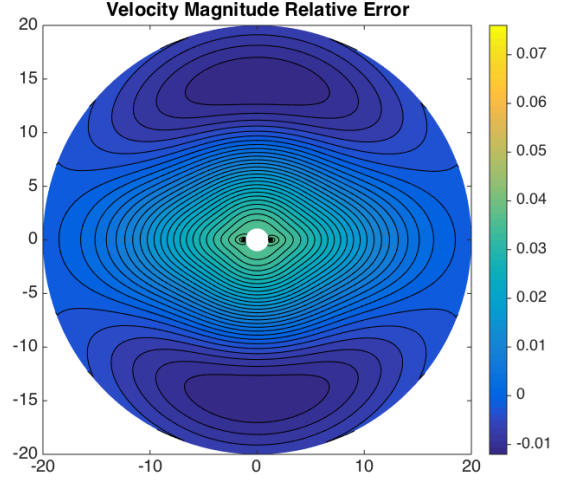


FIG. 3: Relative error of fluid speed for the numerical solution as compared with the analytic solution (Eq. 5) on domain of radius 20.

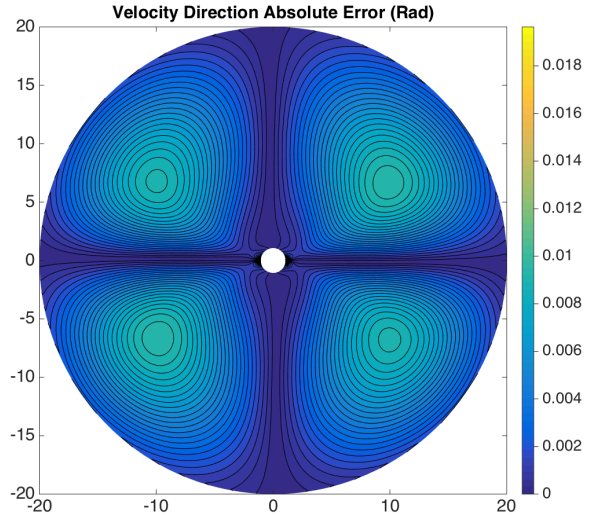


FIG. 4: Absolute error of fluid direction for the numerical solution as compared with the analytic solution (Eq. 5) on domain of radius 20.

tion profile from the advection-diffusion equation. Our eventual aim is to find the first passage probability of a dissolved molecule released at position (ξ', θ') through the inner boundary at $\xi = 1$. To accomplish this, we solve the advection-diffusion equation using the known velocity profile. In this section we first discuss a numerical solution of the problem, and then compare our results to an analytic approximation.

For an incompressible fluid, the advection-diffusion equation reads as

$$\frac{\partial C}{\partial t} + \mathbf{U} \cdot \nabla C = D \nabla^2 C \quad (6)$$

where D is the diffusion coefficient for the molecule of

interest, C is the molecular concentration, and t is time. Defining the dimensionless concentration $c = CR^2$, time $\tau = (Dt)/R^2$, and Péclet number $\text{Pe} = (RU_\infty)/D$, the dimensionless form of Eq. (6) in plane polar coordinates is

$$\frac{\partial c}{\partial \tau} + \text{Pe} \left(u_\xi \frac{\partial c}{\partial \xi} + \frac{u_\theta}{\xi} \frac{\partial c}{\partial \theta} \right) = \frac{\partial^2 c}{\partial \xi^2} + \frac{1}{\xi} \frac{\partial c}{\partial \xi} + \frac{1}{\xi^2} \frac{\partial^2 c}{\partial \theta^2}. \quad (7)$$

In order to solve Eq. (7) numerically, we replace the derivatives with their finite-difference counterparts,

$$\begin{aligned} c_{i,j}^{k+1} = 2h_\tau & \left[-\text{Pe} \left(u_\xi \frac{c_{i+1,j}^k - c_{i,j}^k}{2h_\xi} + \frac{u_\theta}{\xi} \frac{c_{i,j+1}^k - c_{i,j}^k}{2h_\theta} \right) \right. \\ & + \frac{c_{i+1,j}^k - 2c_{i,j}^k + c_{i-1,j}^k}{h_\xi^2} + \frac{1}{\xi} \frac{c_{i+1,j}^k - c_{i,j}^k}{2h_\xi} \\ & \left. + \frac{1}{\xi^2} \frac{c_{i,j+1}^k - 2c_{i,j}^k + c_{i,j-1}^k}{h_\theta^2} \right] + c_{i,j}^k. \end{aligned} \quad (8)$$

Here $c_{i,j}^k$ is the value of the concentration at the location indexed by i, j at time k and h_τ is the time step. For further details on the computational grid employed, see the Appendix. Since our goal is to find the concentration profile as $\tau \rightarrow \infty$, we could set the time derivative in Eq. (7) to zero and solve in a manner similar to that used for the Stokes equation, but a simpler approach exists. We use an explicit finite difference scheme where the concentration at time $k+1$ is computed from the concentration at time k as shown in Eq. (8). This is continued until the change in the concentration field is below some small value. The first-passage probability is then just the flux through the inner absorbing boundary divided by the sum of the flux through the inner and outer boundaries.

Algorithm 1 Explicit Finite-Difference scheme to find the Concentration Profile and First-Passage Probability

```

while correction > Some small number do
  for all  $i, j$  do
    if  $i = 1$  then
       $c_{1,j}^{k+1} = 0$ 
    end if
    if  $i = imax$  then
       $c_{imax,j}^{k+1} = 0$ 
    end if
    Find  $c_{i,j}^{k+1}$  using Eq. (8)
    if  $|c_{i,j}^{k+1} - c_{i,j}^k| > correction$  then
       $correction = |c_{i,j}^{k+1} - c_{i,j}^k|$ 
    end if
     $c_{i,j}^k = c_{i,j}^{k+1}$ 
  end for
end while

```

$$\Pi = \int_0^{2\pi} d\theta \left. \xi \frac{\partial c}{\partial \xi} \right|_{\xi=1} / \int_0^{2\pi} d\theta \left(\left. \xi \frac{\partial c}{\partial \xi} \right|_{\xi=1} - \left. \xi \frac{\partial c}{\partial \xi} \right|_{\xi=\xi_{max}} \right)$$

With the numerical solution in hand, we turn to discuss

an approximate analytical approach to the problem. The basic idea is to use methods common to boundary layer problems to find the leading order solution of Eq. (7) with the boundary conditions given. The approach is similar to that outlined in [7], but the dimensionality and nature of the underlying fluid model is different here. In terms of the small parameter $\alpha = 1/\text{Pe}$, the advection-diffusion equation for the concentration field is

$$\alpha \frac{\partial c}{\partial \tau} + u_\xi \frac{\partial c}{\partial \xi} + \frac{u_\theta}{\xi} \frac{\partial c}{\partial \theta} = \alpha \left(\frac{\partial^2 c}{\partial \xi^2} + \frac{1}{\xi} \frac{\partial c}{\partial \xi} + \frac{1}{\xi^2} \frac{\partial^2 c}{\partial \theta^2} \right). \quad (9)$$

We first rescale the radial variable $\xi = 1 + \alpha^n \rho$ to stretch out the boundary layer. The dimensionless time is rescaled as $\tau = \alpha^m T$, but we do not rescale the angular variable θ . Dominant balance [17] determines the value of exponents $n = 1/3$ and $m = 2/3$. By making this choice of exponents, in a perturbative expansion for the concentration, $c = \sum_{k=0}^{\infty} \alpha^{k/3} c_k$, the equation governing c_0 will contain temporal, advective, and diffusive terms. The rescaled advection-diffusion equation is

$$\begin{aligned} \frac{\partial c}{\partial T} + \alpha^{-2/3} u_\xi \frac{\partial c}{\partial \rho} + \frac{\alpha^{-1/3}}{1 + \alpha^{1/3} \rho} u_\theta \frac{\partial c}{\partial \theta} \\ = \frac{\partial^2 c}{\partial \rho^2} + \frac{\alpha^{1/3}}{1 + \alpha^{1/3} \rho} \frac{\partial c}{\partial \rho} + \frac{\alpha^{2/3}}{(1 + \alpha^{1/3} \rho)^2} \frac{\partial^2 c}{\partial \theta^2}. \end{aligned} \quad (10)$$

Note that the velocity components $u_\xi \sim O(\alpha^{2/3})$ and $u_\theta \sim O(\alpha^{1/3})$ depend on α when expressed in terms of the radial variable ρ . The physical thickness of the concentration boundary layer is $\ell = R \alpha^{1/3}$.

Inserting the perturbative expansion into Eq. (10) and collecting terms of the same order in $\alpha^{1/3}$, the result is a system of coupled equations for the $\{c_k\}$. Defining $\mu = \cos \theta$ and $\beta = 2(Q^2 - 1)/G(Q)$, the lowest order governing equations are

$$\frac{\partial c_0}{\partial T} + \frac{1}{2} \beta \rho^2 \mu \frac{\partial c_0}{\partial \rho} + \beta \rho (1 - \mu^2) \frac{\partial c_0}{\partial \mu} - \frac{\partial^2 c_0}{\partial \rho^2} = 0, \quad (11)$$

$$\frac{\partial c_1}{\partial T} + \frac{1}{2} \beta \rho^2 \mu \frac{\partial c_1}{\partial \rho} + \beta \rho (1 - \mu^2) \frac{\partial c_1}{\partial \mu} - \frac{\partial^2 c_1}{\partial \rho^2} = \frac{\partial c_0}{\partial \rho}. \quad (12)$$

A perturbation series is obtained by calculating c_0 from Eq. (11), and using the solution to solve the inhomogeneous equation for c_1 , Eq. (12). Additional corrections can in principle be calculated from the tower of governing equations [18]. In what follows we will only attempt a solution of the zeroth order equation, which as we will see is in reasonable agreement with the numerical results.

A common method in this type of boundary layer problem [19, 20] is to define similarity variables $\eta = \rho/g$ and $\chi = T/g^2$, where $g(\mu)$ encapsulates the angular dependence of the boundary layer. The zeroth-order equation transforms into

$$\frac{\partial c_0}{\partial \chi} + \beta \eta^2 \left(\frac{1}{2} \mu g^3 - (1 - \mu^2) g^2 \frac{dg}{d\mu} \right) \frac{\partial c_0}{\partial \eta} - \frac{\partial^2 c_0}{\partial \eta^2} + \beta (1 - \mu^2) \eta g^3 \frac{\partial c_0}{\partial \mu} = 0. \quad (13)$$

If the term in large parentheses is equal to a constant,

$$\frac{\mu g^3}{2} - (1 - \mu^2) g^2 \frac{dg}{d\mu} = \Delta, \quad (14)$$

the governing equation is separable in the η and μ coordinates. However, in what follows we will only consider solutions in which the angular dependence is captured by the boundary layer variables and neglect the explicit angular derivative in the governing equation, i.e. $\frac{\partial c_0}{\partial \mu} = 0$. This approximation was also made in [7], although the solutions for $g(\mu)$ are different in the two cases. This simplifies our governing equation significantly to

$$\frac{\partial c_0}{\partial \chi} + \beta \eta^2 \Delta \frac{\partial c_0}{\partial \eta} - \frac{\partial^2 c_0}{\partial \eta^2} = 0. \quad (15)$$

Without loss of generality, we make the choice $\Delta = -1$. The differential equation for $g(\mu)$ is readily solved, with Υ a constant of integration,

$$g(\mu) = 3^{1/3} (1 - \mu^2)^{-1/4} \left(\mu {}_2F_1 \left[\frac{1}{4}, \frac{1}{2}, \frac{3}{2}, \mu^2 \right] + \Upsilon \right)^{1/3}. \quad (16)$$

The hypergeometric function ${}_2F_1[a, b, c, z]$ is defined by the infinite sum

$${}_2F_1[a, b, c, z] = \sum_{n=0}^{\infty} \frac{(a)_n (b)_n}{(c)_n} \frac{z^n}{n!} \quad (17)$$

where

$$(x)_n = \frac{\Gamma(x+n)}{\Gamma(x)} \quad (18)$$

is the Pochhammer symbol. The integration constant $\Upsilon = {}_2F_1 \left[\frac{1}{4}, \frac{1}{2}, \frac{3}{2}, 1 \right]$ is determined by the condition that $g(\mu)$ be positive and bounded, except at $\mu = \pm 1$ where the boundary-layer scaling may break down.

In Fig. 5 the steady-state solution ($\frac{\partial c_0}{\partial \chi} = 0$) of Eq. (15) is plotted. The boundary conditions for the concentration are perfect absorption at the surface of the cell ($c_0 = 0$ at $\eta = 0$) and a far-field value of c_Q . The solution of Eq. (15) is expressed in terms of the incomplete Gamma function $\Gamma(a, z)$ as

$$c_0 = c_Q \left(1 - \frac{\Gamma \left(\frac{1}{3}, \frac{\beta}{3} \eta^3 \right)}{\Gamma \left(\frac{1}{3} \right)} \right). \quad (19)$$

$$\Gamma(a, z) = \int_z^{\infty} t^{a-1} e^{-t} dt \quad (20)$$

Note the angular dependence of the characteristic concentration plume in the wake of the flow is captured by the boundary layer variable η .

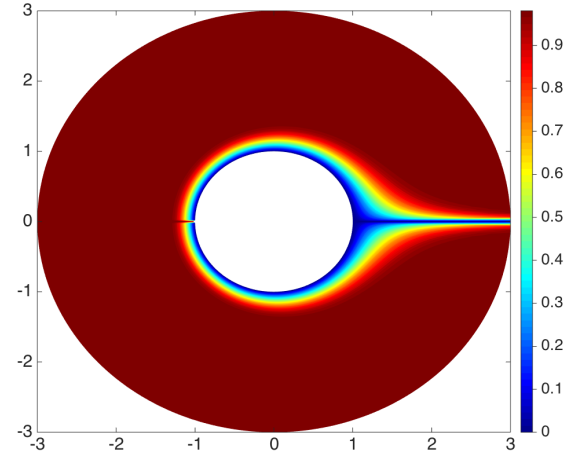


FIG. 5: Concentration profile (c_0/c_Q) for the case of strong advection $Pe = 1000$ and the far field parameter at $Q = 20$.

For the purposes of the first-passage calculation, we consider a spatial domain where all molecules released are eventually captured with probability one. The concentration is defined in the annulus between two perfectly absorbing surfaces, the first at the surface of the circular cell ($\eta = 0$), and a second at some prescribed distance ($\eta = \eta_+$). We define the time-integrated concentration

$$\mathcal{C}_0 = \int_0^{\infty} c_0 d\chi. \quad (21)$$

The equation for \mathcal{C}_0 is

$$c_0(\chi = \infty) - c_0(\chi = 0) - \beta \eta^2 \frac{\partial c_0}{\partial \eta} - \frac{\partial^2 c_0}{\partial \eta^2} = 0. \quad (22)$$

Since all molecules are eventually absorbed, $c_0(\chi = \infty) = 0$. If a molecule is released in the extracellular fluid at position (ξ', θ') , the corresponding initial condition is $c_0(\chi = 0) = \delta^2(\xi - \xi') = \frac{1}{\xi} \delta(\xi - \xi') \delta(\theta - \theta')$.

Writing the initial condition in terms of η , we find

$$\frac{\partial^2 \mathcal{C}_0}{\partial \eta^2} + \beta \eta^2 \frac{\partial \mathcal{C}_0}{\partial \eta} = - \frac{\delta \left(\eta - \frac{g(\mu')}{g(\mu)} \eta' \right) \delta(\theta - \theta')}{\alpha^{1/3} g(\mu) (1 + \alpha^{1/3} g(\mu) \eta)}. \quad (23)$$

To solve Eq. (23), note that the two independent solutions to the homogeneous equation are a constant and $\Gamma\left(\frac{1}{3}, \frac{\beta}{3}\eta^3\right)$. Using perfectly absorbing boundary conditions at $\eta = 0$ and $\eta = \eta_+$, the solution for \mathcal{C}_0 is

$$\mathcal{C}_0 = \mathcal{I} \left[\Gamma\left(\frac{1}{3}, \frac{\beta}{3}\eta_-^3\right) - \Gamma\left(\frac{1}{3}\right) \right] \\ \times \left[\Gamma\left(\frac{1}{3}, \frac{\beta}{3}\eta_+^3\right) - \Gamma\left(\frac{1}{3}, \frac{\beta}{3}\eta_+^3\right) \right]. \quad (24)$$

Here η_- (η_+) is the smaller (larger) of η and η' . To determine the constant \mathcal{I} , we integrate both sides of the governing equation $\int_0^{2\pi} d\theta g(\mu) \int_{\eta'-\epsilon}^{\eta'+\epsilon} d\eta$ to determine the discontinuity in the first derivative of \mathcal{C}_0 ,

$$\frac{\partial \mathcal{C}_0}{\partial \eta} \bigg|_{\eta=\eta'-\epsilon}^{\eta=\eta'+\epsilon} = -\frac{1}{G\alpha^{1/3}(1+\alpha^{1/3}g(\mu')\eta')} \quad (25)$$

where $G = \int_0^{2\pi} d\theta g(\mu)$. The factor of $g(\mu)$ in the integration to determine the discontinuity was incorrectly omitted in [7], it is needed to ensure the proper normalization,

$$\mathcal{I} = \frac{e^{\frac{\beta}{3}\eta'^3}}{(9\beta\alpha)^{1/3}G(1+\alpha^{1/3}g(\mu')\eta') \left[\Gamma\left(\frac{1}{3}, \frac{\beta}{3}\eta_+^3\right) - \Gamma\left(\frac{1}{3}\right) \right]}. \quad (26)$$

In terms of the original variables, the first-passage probability is calculated as

$$\Pi_0 = \int_0^\infty d\tau \int_0^{2\pi} d\theta \xi \frac{\partial \mathcal{C}_0}{\partial \xi} \bigg|_{\xi=1}. \quad (27)$$

The result can be written in terms of the boundary layer variable η and the time-integrated concentration \mathcal{C}_0 as

$$\Pi_0 = \alpha^{1/3} \int_0^{2\pi} d\theta g(\mu) \frac{\partial \mathcal{C}_0}{\partial \eta} \bigg|_{\eta=0}. \quad (28)$$

Performing the angular integration we arrive at

$$\Pi_0 = \frac{\left[\Gamma\left(\frac{1}{3}, \frac{\beta}{3}\eta'^3\right) - \Gamma\left(\frac{1}{3}, \frac{\beta}{3}\eta_+^3\right) \right] e^{\frac{\beta}{3}\eta'^3}}{\left[\Gamma\left(\frac{1}{3}\right) - \Gamma\left(\frac{1}{3}, \frac{\beta}{3}\eta_+^3\right) \right] (1+\alpha^{1/3}g(\mu')\eta')}. \quad (29)$$

Moving the outer absorber η_+ out to infinity and writing the result back in terms of ξ' yields the final result,

$$\Pi_0 = \frac{\Gamma\left(\frac{1}{3}, \frac{\beta(\xi'-1)^3}{3\alpha g(\mu')^3}\right) e^{\frac{\beta(\xi'-1)^3}{3\alpha g(\mu')^3}}}{\Gamma\left(\frac{1}{3}\right) \xi'}. \quad (30)$$

Note that the final result is properly normalized as $\Pi_0(\xi' = 1) = 1$. To make a comparison with the numerical solution for a ring of point sources, we calculate the average first-passage probability, $\langle \Pi_0 \rangle = \frac{1}{2\pi} \int_0^{2\pi} d\theta \Pi_0$ from Eq. (30). Figure 6 shows a comparison of the nu-

merical result for the first-passage probability produced by Algorithm 1 and the analytic approximation. The result for the first-passage probability is in quantitative agreement with the numerical result provided the source is not located too far outside of the concentration boundary layer.

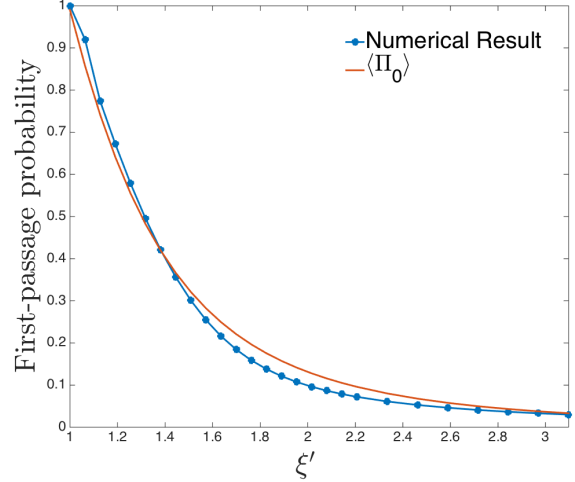


FIG. 6: First-passage probability $\langle \Pi_0 \rangle$ for a ring source at ξ' and the numerically computed first-passage probability for $\text{Pe} = 100$.

To make contact with the motivations for the study discussed in the introduction, note that a physical microvilli length of $4 \mu\text{m}$ corresponds to a source location of $\xi' = 1.1$ in Fig. 6, in which case the numerical and analytical approaches are in good agreement. It is worth noting that much of this calculation carries over to the more realistic case of a spherical embryo in a three-dimensional flow field, as can be seen by comparing this result to the result from [7]. Properly normalized, the result of [7] is almost identical in structure to Eq. (30), despite the fact that the three-dimensional fluid model considered there is very different than the two-dimensional case treated in this paper. The meaning of the parameter β is different in the two and three-dimensional fluid models, and the equation for $g(\mu)$ changes, but the functional form of the first-passage probability is the essentially the same. The only other difference is that, as a consequence of dimensionality, in a three-dimensional model, the factor of ξ' in the denominator of Eq. (30) becomes $(\xi')^2$. An extension of the numerical methods presented here to the three-dimensional case and the associated comparison to the analytic approximation is a significant task for future research.

IV. CONCLUSION

Motivated by a mass transport problem during sea urchin development, we considered a simple two-

dimensional model to study the first-passage problem for an advection-diffusion equation at small Reynolds number and large Péclet number. Numerical approaches to solving the advection-diffusion equation based on a modified Gauss-Seidel algorithm and explicit finite-differencing were compared to an analytic approximation based on a rescaling of the concentration boundary layer. For large Péclet number we find quantitative agreement between the approaches. As the Péclet number is reduced, the analytic approximation continues to capture the qualitative behavior of the first-passage probability, but deviates from the numerical results. In problems with $\text{Pe} \sim 1$ the numerical approach is preferred. The regime of validity for the analytic approximation might be improved by a more detailed investigation of the complete zeroth order governing equation, Eq. (13), or by continuing the perturbation program beyond the leading order. This is a potential direction for future research.

V. ACKNOWLEDGEMENTS

This work was supported by faculty startup grant U035843 from the College of Arts, Sciences, and Letters at the University of Michigan-Dearborn.

VI. APPENDIX: GAUSS-SEIDEL METHOD

Our first step towards using a linear numerical method is to replace the derivatives in the governing equations with their corresponding finite difference approximations. This action serves to convert the system of coupled differential equations into a large linear system having the familiar form $\mathbf{Ax} = \mathbf{b}$.

Second order accurate finite difference approximations are used to replace the derivatives in Eqs. (3) and (4). Centered finite differences of first and second derivatives take the form [21]

$$\begin{aligned} \left(\frac{\partial u}{\partial \xi} \right)_{i,j} &= \frac{u_{i+1,j} - u_{i-1,j}}{2h_\xi} \\ \left(\frac{\partial^2 u}{\partial \xi^2} \right)_{i,j} &= \frac{u_{i+1,j} - 2u_{i,j} + u_{i-1,j}}{h_\xi^2} \end{aligned} \quad (31)$$

while one sided finite differences take the form

$$\begin{aligned} \left(\frac{\partial u}{\partial \xi} \right)_{i,j} &= \frac{-3u_{i,j} + 4u_{i+1,j} - u_{i+2,j}}{2h_\xi} \\ \left(\frac{\partial^2 u}{\partial \xi^2} \right)_{i,j} &= \frac{2u_{i,j} - 5u_{i+1,j} + 4u_{i+2,j} - u_{i+3,j}}{h_\xi^2}. \end{aligned} \quad (32)$$

The index i represents steps of size h_ξ in the direction of $\hat{\xi}$ while the index j represents steps of size h_θ in the direction of $\hat{\theta}$. Centered finite differences are used away from boundaries where the data points $i-1$ and $i+1$ or $j-1$ and $j+1$ all lie within the domain. One sided

finite differences are used at boundaries where some of the neighboring data points do not exist.

We choose a staggered grid on which to evaluate each of the dependent variables: u_ξ , u_θ , and γ . The use of a staggered rather than co-located grid keeps the variables coupled during the iterative methods of solution used later. The plane polar domain is divided into a series of wedge shaped cells. Each cell contains a group of the dependent variables at index i, j . The pressure is evaluated at the center of a cell while the radial and angular components of the velocity are evaluated on the respective upper and right boundaries of a cell.

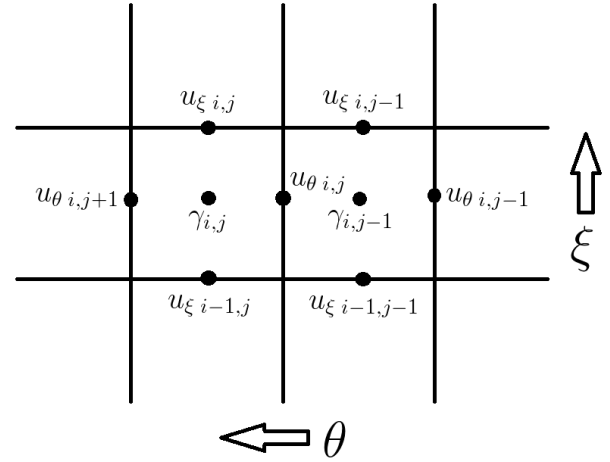


FIG. 7: A small patch of the computational grid. The pressure and velocity components at index i, j are shown occupying the upper right corner of a cell along with neighboring indices. The arrows show the direction of increasing ξ and θ values.

With the computational grid now chosen, finite difference approximations can be used in place of the derivatives in Eqs. (3) and (4). Within each cell not at the boundary of the domain, Eq. (3a) is evaluated at the location of $u_\xi_{i,j}$ as

$$\begin{aligned} \text{Re} \left[\frac{u_{\xi,i+1,j} - 2u_{\xi,i,j} + u_{\xi,i-1,j}}{h_\xi^2} + \frac{u_{\xi,i+1,j} - u_{\xi,i-1,j}}{2h_\xi h_\theta} \right. \\ \left. - \frac{u_{\xi,i,j}}{\xi^2} + \frac{u_{\xi,i,j+1} - 2u_{\xi,i,j} + u_{\xi,i,j-1}}{\xi^2 h_\theta^2} \right. \\ \left. - \frac{(u_{\theta,i,j+1} + u_{\theta,i+1,j+1}) - (u_{\theta,i,j} + u_{\theta,i+1,j})}{\xi^2 h_\theta} \right] \\ - \frac{\gamma_{i+1,j} - \gamma_{i,j}}{h_\xi} = 0, \end{aligned} \quad (33)$$

Eq. (3b) is evaluated at the location of $u_{\theta i,j}$ as

$$\begin{aligned} \text{Re} \left[\frac{u_{\theta i+1,j} - 2u_{\theta i,j} + u_{\theta i-1,j}}{h_{\xi}^2} + \frac{u_{\theta i+1,j} - u_{\theta i-1,j}}{2h_{\xi}\xi_*} \right. \\ - \frac{u_{\theta i,j}}{\xi_*^2} + \frac{u_{\theta i,j+1} - 2u_{\theta i,j} + u_{\theta i,j-1}}{\xi_*^2 h_{\theta}^2} \\ \left. + \frac{(u_{\xi i-1,j} + u_{\xi i,j}) - (u_{\xi i-1,j-1} + u_{\xi i,j-1})}{\xi_*^2 h_{\theta}} \right] \\ - \frac{\gamma_{i,j} - \gamma_{i,j-1}}{\xi_* h_{\theta}} = 0 \end{aligned} \quad (34)$$

where $\xi_* = \xi - h_{\xi}/2$, and Eq. (4) is evaluated at the location of $\gamma_{i,j}$ as

$$\frac{u_{\xi i,j} - u_{\xi i-1,j}}{h_{\xi}} + \frac{u_{\xi i,j} + u_{\xi i-1,j}}{2\xi_*} + \frac{u_{\theta i,j+1} - u_{\theta i,j}}{\xi_* h_{\theta}} = 0. \quad (35)$$

Notice that the use of a staggered grid causes some of the adjacent data points to be offset from their needed locations. A simple work-around is to average the values of the surrounding data points to find an acceptable value at the required location. This is done for the angular derivative of u_{θ} in Eq. (33), the angular derivative of u_{ξ} in Eq. (34), and the value of $u_{\xi i-1/2,j}$ in Eq. (35).

For computational cells which do lie against the boundary of the domain, boundary conditions must be imposed and one sided finite differences used where adjacent data points are missing. At the inner boundary where $\xi = 1$, $u_{\xi 1,j} = 0$ and $u_{\theta 1,j} + u_{\theta 2,j} = 0$. Again, averaging is being employed here since data points in u_{θ} are offset from the boundary. With conditions set on the velocity components, the pressure can be calculated by using Eq. (33) and swapping out the centered finite differences in ξ with one sided differences giving us $(-5u_{\xi 2,j} + 4u_{\xi 3,j} - u_{\xi 4,j})/\text{Re } h_{\xi}^2 - (\gamma_{2,j} - \gamma_{1,j})/h_{\xi} = 0$. At the outer boundary where $\xi = Q$, the constraints are $u_{\xi imax,j} = \cos((j + 1/2)h_{\theta})$, $u_{\theta imax,j} = -\sin(jh_{\theta})$, and $\gamma_{imax,j} = 0$.

It is often informative to write the linear system in matrix form. We begin by defining the vector

$$\mathcal{X}_{i,j} = \begin{bmatrix} u_{\xi i,j} \\ u_{\theta i,j} \\ \gamma_{i,j} \end{bmatrix}. \quad (36)$$

At points away from domain boundaries, the linear system can now be written in block matrix form with the coefficient matrix built from seven 3×3 sub-matrices,

$$\begin{bmatrix} \vdots & \ddots & & \ddots & & \ddots & \\ \vdots & & & & & & \vdots \\ 0 & \dots & \mathbb{E} & \mathbb{F} & \dots & \mathbb{G} & \mathbb{D} & \mathbb{Q} & \dots & \mathbb{R} & \mathbb{S} & 0 & 0 & \dots & 0 \\ 0 & \dots & 0 & \mathbb{E} & \mathbb{F} & \dots & \mathbb{G} & \mathbb{D} & \mathbb{Q} & \dots & \mathbb{R} & \mathbb{S} & 0 & \dots & 0 \\ 0 & \dots & 0 & 0 & \mathbb{E} & \mathbb{F} & \dots & \mathbb{G} & \mathbb{D} & \mathbb{Q} & \dots & \mathbb{R} & \mathbb{S} & \dots & 0 \\ \vdots & & & \ddots & & & \ddots & & & \ddots & & & \vdots & & \vdots \end{bmatrix} \begin{bmatrix} \mathcal{X}_{i-1,j-1} \\ \mathcal{X}_{i-1,j} \\ \vdots \\ \mathcal{X}_{i,j-1} \\ \mathcal{X}_{i,j} \\ \mathcal{X}_{i,j+1} \\ \vdots \\ \mathcal{X}_{i+1,j} \\ \mathcal{X}_{i+1,j+1} \\ \vdots \end{bmatrix} = \begin{bmatrix} \vdots \\ 0 \\ \vdots \end{bmatrix}. \quad (37)$$

$$\mathbb{D} = \begin{bmatrix} \frac{1}{\text{Re}} \left(\frac{-2}{h_{\xi}^2} - \frac{1}{\xi_*^2} - \frac{2}{\xi_*^2 h_{\theta}^2} \right) & \frac{1}{\text{Re} \xi_*^2 h_{\theta}} & \frac{1}{h_{\xi}} \\ \frac{1}{\text{Re} \xi_*^2 h_{\theta}} & \frac{1}{\text{Re}} \left(\frac{-2}{h_{\xi}^2} - \frac{1}{\xi_*^2} - \frac{2}{\xi_*^2 h_{\theta}^2} \right) & -\frac{1}{\xi_* h_{\theta}} \\ \frac{1}{h_{\xi}} + \frac{1}{2\xi_*} & -\frac{1}{\xi_* h_{\theta}} & 0 \end{bmatrix} \quad (38)$$

$$\mathbb{E} = \begin{bmatrix} 0 & 0 & 0 \\ -\frac{1}{\text{Re} \xi_*^2 h_{\theta}} & 0 & 0 \\ 0 & 0 & 0 \end{bmatrix} \quad (39)$$

$$\mathbb{F} = \begin{bmatrix} \frac{1}{\text{Re}} \left(\frac{1}{h_{\xi}^2} - \frac{1}{2h_{\xi}\xi_*} \right) & 0 & 0 \\ \frac{1}{\text{Re} \xi_*^2 h_{\theta}} & \frac{1}{\text{Re}} \left(\frac{1}{h_{\xi}^2} - \frac{1}{2h_{\xi}\xi_*} \right) & 0 \\ -\frac{1}{h_{\xi}} + \frac{1}{2\xi_*} & 0 & 0 \end{bmatrix} \quad (40)$$

$$\mathbb{G} = \begin{bmatrix} \frac{1}{\text{Re} \xi_*^2 h_{\theta}^2} & 0 & 0 \\ \frac{1}{\text{Re} \xi_*^2 h_{\theta}} & \frac{1}{\text{Re} \xi_*^2 h_{\theta}^2} & \frac{1}{\xi_* h_{\theta}} \\ 0 & 0 & 0 \end{bmatrix} \quad (41)$$

$$\mathbb{Q} = \begin{bmatrix} \frac{1}{\text{Re} \xi^2 h_\theta^2} & -\frac{1}{\text{Re} \xi^2 h_\theta} & 0 \\ 0 & \frac{1}{\text{Re} \xi_*^2 h_\theta^2} & 0 \\ 0 & \frac{1}{\xi_* h_\theta} & 0 \end{bmatrix} \quad (42)$$

$$\mathbb{R} = \begin{bmatrix} \frac{1}{\text{Re}} \left(\frac{1}{h_\xi^2} + \frac{1}{2h_\xi \xi} \right) & \frac{1}{\text{Re} \xi^2 h_\theta} & -\frac{1}{h_\xi} \\ 0 & \frac{1}{\text{Re}} \left(\frac{1}{h_\xi^2} + \frac{1}{2h_\xi \xi_*} \right) & 0 \\ 0 & 0 & 0 \end{bmatrix} \quad (43)$$

$$\mathbb{S} = \begin{bmatrix} 0 & -\frac{1}{\text{Re} \xi^2 h_\theta} & 0 \\ 0 & 0 & 0 \\ 0 & 0 & 0 \end{bmatrix} \quad (44)$$

Notice that the coefficient matrix in Eq. (37) is a sparse, diagonally banded matrix. There are a number of well known algorithms for solving such linear systems. Since we are generally interested in solving for the flow profile corresponding to a particular situation, we aim for simplicity over efficiency when choosing an algorithm for solving the system.

We choose a block form of the Gauss-Seidel method for solving the system given in Eq. (37). The algorithm is relatively fast and less resource intensive when compared to direct methods of solution such as Gaussian elimination. Better still, the method is one of the simplest of its kind to implement [13]. Assuming the standard notation $\mathbf{Ax} = \mathbf{b}$ for Eq. (37) with \mathcal{A} , \mathcal{X} , and \mathcal{B} representing the corresponding sub-matrices and sub-vectors, the block Gauss-Seidel algorithm is

$$\mathcal{X}_m^{k+1} = \frac{1}{\mathcal{A}_{mm}} \left(\mathcal{B}_m - \sum_{n < m} \mathcal{A}_{mn} \mathcal{X}_n^{k+1} - \sum_{n > m} \mathcal{A}_{mn} \mathcal{X}_n^k \right). \quad (45)$$

The subscript on vector \mathcal{X}_m in Eq. (45) relates to that on vector $\mathcal{X}_{i,j}$ in Eq. (36) by $m = (i-1) \cdot imax + j$.

The solution of Eq. (37) is found by repeatedly applying Eq. (45) until the change in each $\mathcal{X}_{i,j}$ is below some small value. At each iteration k , the vector $\mathcal{X}_{i,j}^{k+1}$ is calculated using Eq. (46). Algorithm 2 shows how to implement the Gauss-Seidel algorithm for finding the flow profile.

$$\mathcal{X}_{i,j}^{k+1} = \mathbb{D}^{-1} \left[\begin{array}{l} -\frac{1}{\text{Re}} \left(\frac{u_{\xi, i+1,j} + u_{\xi, i-1,j}}{h_\xi^2} + \frac{u_{\xi, i+1,j} - u_{\xi, i-1,j}}{2h_\xi \xi} + \frac{u_{\xi, i,j+1} + u_{\xi, i,j-1}}{\xi^2 h_\theta^2} - \frac{u_{\theta, i,j+1} + u_{\theta, i+1,j+1} - u_{\theta, i+1,j}}{\xi^2 h_\theta} \right) + \frac{\gamma_{i+1,j}}{h_\xi} \\ -\frac{1}{\text{Re}} \left(\frac{u_{\theta, i+1,j} + u_{\theta, i-1,j}}{h_\xi^2} + \frac{u_{\theta, i+1,j} - u_{\theta, i-1,j}}{2h_\xi \xi_*} + \frac{u_{\theta, i,j+1} + u_{\theta, i,j-1}}{\xi_*^2 h_\theta^2} + \frac{u_{\xi, i-1,j} - u_{\xi, i-1,j-1} + u_{\xi, i,j-1}}{\xi_*^2 h_\theta} \right) - \frac{\gamma_{i,j-1}}{\xi_* h_\theta} \\ \frac{u_{\xi, i-1,j}}{h_\xi} - \frac{u_{\xi, i-1,j}}{2\xi_*} - \frac{u_{\theta, i,j+1}}{\xi_* h_\theta} \end{array} \right] \quad (46)$$

Algorithm 2 GS Method to find the Flow Profile

```

while correction > Some small number do
  for all i, j do
    if i = 1 then
      Find  $\mathcal{X}_{1,j}^{k+1}$  using surface BCs
    end if
    if i = imax then
      Find  $\mathcal{X}_{imax,j}^{k+1}$  using outer BCs
    end if
    Find  $\mathcal{X}_{i,j}^{k+1}$  using Eq. (46)
    if  $|\mathcal{X}_{i,j}^{k+1} - \mathcal{X}_{i,j}^k|_\infty > \text{correction}$  then
      correction =  $|\mathcal{X}_{i,j}^{k+1} - \mathcal{X}_{i,j}^k|_\infty$ 
    end if
     $\mathcal{X}_{i,j}^k = \mathcal{X}_{i,j}^{k+1}$ 
  end for
end while

```

[1] B. J. Cole, A. Hamdoun, and D. Epel, “Cost, effectiveness and environmental relevance of multidrug trans-

porters in sea urchin embryos,” *Journal of Experimental Biology*, vol. 216, no. 20, pp. 3896–3905, 2013.

- [2] M. B. Short, C. A. Solari, S. Ganguly, T. R. Powers, J. O. Kessler, and R. E. Goldstein, “Flows driven by flagella of multicellular organisms enhance long-range molecular transport,” *Proceedings of the National Academy of Sciences*, vol. 103, no. 22, pp. 8315–8319, 2006.
- [3] K. Whalen, A. M. Reitzel, and A. Hamdoun, “Actin polymerization controls the activation of multidrug efflux at fertilization by translocation and fine-scale positioning of abcb1 on microvilli,” *Molecular biology of the cell*, vol. 23, no. 18, pp. 3663–3672, 2012.
- [4] X. Song. PhD thesis, Indiana University, 2008.
- [5] S. Vogel, *Life in moving fluids: the physical biology of flow*. Princeton University Press, 1994.
- [6] T. Gökirmak, J. P. Campanale, L. E. Shipp, G. W. Moy, H. Tao, and A. Hamdoun, “Localization and substrate selectivity of sea urchin multidrug (mdr) efflux transporters,” *Journal of Biological Chemistry*, vol. 287, no. 52, pp. 43876–43883, 2012.
- [7] N. A. Licata and A. Clark, “Fluid flow enhances the effectiveness of toxin export by aquatic microorganisms: a first-passage perspective on microvilli and the concentration boundary layer,” *Physical Review*, vol. 91, no. 012709, 2015.
- [8] H. C. Berg and E. M. Purcell, “Physics of chemoreception,” *Biophysical journal*, vol. 20, no. 2, p. 193, 1977.
- [9] G. K. Batchelor, *An Introduction to Fluid Dynamics*. Cambridge University Press, 1967.
- [10] W. S. Janna, *Introduction to Fluid Mechanics*. PWS Publishing Company, 1993.
- [11] R. H. P. John C. Tannehill, Dale A. Anderson, *Computational Fluid Mechanics and Heat Transfer*. Taylor and Francis, second ed., 1997.
- [12] O. Zikanov, *Essential Computational Fluid Dynamics*. John Wiley and Sons, 2010.
- [13] S. Biringen and C.-Y. Chow, *Introduction to Computational Fluid Mechanics by Example*. John Wiley and Sons, 2011.
- [14] S. Redner, *A guide to first-passage processes*. Cambridge University Press, 2001.
- [15] D. Pnueli and C. Gutfinger, *Fluid Mechanics*. Cambridge University Press, 1992.
- [16] K. McDonald, “Patterns in early embryonic motility: Effects of size and environmental temperature on vertical velocities of sinking and swimming echinoid blastulae,” *Biol. Bull.*, vol. 207, p. 93, 2004.
- [17] L.-Y. Chen, N. Goldenfeld, and Y. Oono, “Renormalization group and singular perturbations: Multiple scales, boundary layers, and reductive perturbation theory,” *Phys. Rev. E*, vol. 54, pp. 376–394, Jul 1996.
- [18] J. Veysey and N. Goldenfeld, “Simple viscous flows: From boundary layers to the renormalization group,” *Rev. Mod. Phys.*, vol. 79, pp. 883–927, Jul 2007.
- [19] V. Magar, T. Goto, and T. J. Pedley, “Nutrient uptake by a selfpropelled steady squirmer,” *Q. J. Mech. Appl. Math.*, vol. 56, pp. 65–91, 2003.
- [20] V. Magar and T. J. Pedley, “Average nutrient uptake by a self-propelled unsteady squirmer,” *Journal of Fluid Mechanics*, vol. 539, pp. 93–112, 9 2005.
- [21] B. Fornberg, “Generation of finite difference formulas on arbitrarily spaced grids,” *Mathematics of Computation*, vol. 51, no. 184, pp. 699–706, 1988.